

Revised crystal structure and electronic properties of high dielectric $\text{Ba}(\text{Fe}_{1/2}\text{Nb}_{1/2})\text{O}_3$ ceramics

Rajyavardhan Ray,^{1,2} A. K. Himanshu,^{3,4} Golak K. Mandal,⁵ Uday Kumar,⁶ S. N. Jha,⁷
N. Patra,⁸ D. Bhattacharya,⁸ A. B. Shinde,⁹ Manuel Richter,^{1,2} and P. S. R. Krishna⁹

¹*Leibniz IFW Dresden, Helmholtzstr. 20, 01069 Dresden, Germany.*

²*Dresden Center for Computational Materials Science (DCMS), TU Dresden, 01062 Dresden, Germany.**

³*Variable Energy Cyclotron Center (VECC), DAE, 1/AF Bidhannagar, Kolkata, India 700064.*

⁴*Homi Bhabha National Institute, Mumbai, India 400094.†*

⁵*Department of Physics, T.M. Bhagalpur University, Bhagalpur, Bihar, India 812007*

⁶*Department of Physics, NIT Jamshedpur, Jamshedpur, Jharkhand, India 831014*

⁷*Raja Ramanna Center for Advanced Technology (RRCAT), Indore, India 452013*

⁸*Bhabha Atomic Research Center (BARC), Trombay, Mumbai, India 400085*

⁹*Solid State Physics Division, Bhabha Atomic Research Center (BARC), Trombay, Mumbai, India 400085*

(Dated: December 17, 2021)

$\text{Ba}(\text{Fe}_{1/2}\text{Nb}_{1/2})\text{O}_3$ ceramics are considered to be promising for technological applications owing to their high dielectric constant over a wide range of temperatures. However, there exists considerable discrepancy over the structural details. We address this discrepancy through a combined x-ray diffraction at room temperature and neutron powder diffraction measurements in the range from 5K up to room temperature, supplemented by a comparative analysis of the earlier reported structures. Our study reveals a cubic structure with space group $Pm\bar{3}m$ at all measured temperatures. Further, the x-ray near edge structure and extended x-ray absorption fine structure studies on the local environment of the Fe ions is consistent with the cubic symmetry. An appropriate value of U for DFT+ U calculations is obtained by comparison with x-ray absorption spectroscopy, which agrees well with the earlier reported electronic properties.

PACS numbers: 61.50.-f; 61.05.C-, 61.05.F-, 61.10.Ht, 71.15.Mb

I. INTRODUCTION

Members of the perovskite family are known to exhibit a wide variety of intriguing and unusual physical phenomena, thus, finding applications as multiferroics [1, 2], catalytic materials [3], energy storage materials [4, 5] optoelectronic and photovoltaic materials [6, 7], and dielectric resonators and filters [8, 9]. With the general formula ABO_3 (typically, A = alkali or alkaline earth or lanthanide cations & B = transition metal cations), simple perovskites form a 3D network of corner sharing BO_6 octahedra while the A-site cations occupy the interstitial 12-fold coordinated sites between the octahedra. Interestingly, most notable perovskites which are of high technological interest are not simple perovskites but rather complex oxides with two different kinds of B-site cations [10]. Correspondingly, they can be represented with the formula $\text{A}(\text{B}_x\text{B}'_{1-x})\text{O}_3$.

Complex perovskites possessing high dielectric constant over a reasonably large temperature range are of particular interest due to applications as capacitive components, dielectric resonators and filters. Among the earliest known ferroelectric materials is lead magnesium niobate, $\text{Pb}(\text{Mg}_{1/3}\text{Nb}_{2/3})\text{O}_3$ (PMN) [11], which belongs to the 1:2 family ($x = 1/3$). It exhibits a classic dielectric relaxation and was consequently designated as a relaxor ferroelectric. Since then, this [12–14] and related systems have been investigated extensively. Another related compound belonging to the 1:1 family ($x = 1/2$) with Fe and Nb transition metal (TM) cations in the B-site,

$\text{Pb}(\text{Fe}_{1/2}\text{Nb}_{1/2})\text{O}_3$ (PFN) has also attracted considerable attention [15–17]. However, in all these compounds, lead is an important component. Due to formation of lead vacancies resulting from evaporation of lead compounds during synthesis at high temperatures, investigations of stoichiometric compounds are quite challenging. At the same time, lead compounds have harmful impact on humans and environment. Therefore, search for lead-free ceramics with high dielectric constant is of topical interest.

In this article, we focus on barium iron niobate $\text{Ba}(\text{Fe}_{1/2}\text{Nb}_{1/2})\text{O}_3$ (BFN) ceramics. BFN based electroceramics are found to exhibit attractive dielectric and electrical properties over a wide temperature range [11, 18–33]. However, there exist contradicting reports with regard to its structural properties. The structural symmetry of BFN has been reported to be monoclinic [20, 28, 32–36], cubic $Pm\bar{3}m$ [19, 22, 26, 30, 37, 38], as well as face centered cubic $Fm\bar{3}m$ [21–25] at room temperature. Furthermore, any correlation between the synthesis method and the reported structural symmetry is unavailable.

We address this discrepancy over the structure by carrying out a detailed overview of the reported crystal structures and its possible dependence on the choice of synthesis method and parameters. We argue that the source of such a discrepancy is likely due to possible pseudosymmetry of BFN as observed earlier for many other perovskites, and can be resolved through a careful analysis of the X-ray diffraction (XRD) and neutron powder diffraction (NPD) measurements. Subsequently, we obtain the space group symmetry of BFN by carrying out combined XRD and NPD measurements. We find that BFN crystallizes in the cubic $Pm\bar{3}m$ space group (No. 221) at ambient temperature and that the chemical for-

* r.ray@ifw-dresden.de

† akhimanshu@gmail.com

mula matches with the single perovskite $\text{Ba}(\text{Fe}_{1/2}\text{Nb}_{1/2})\text{O}_3$, disagreeing with the earlier reports of monoclinic and cubic $Fm\bar{3}m$ structures. This further implies that the occupation of the B-site by the TM ions Fe and Nb is random. Further details regarding the local structure are obtained using extended x-ray absorption fine structure (EXAFS) and x-ray near edge structure (XANES) spectroscopy.

A detailed investigation of the electronic and optical properties is also carried out using a combination of diffuse reflectance spectroscopy in the UV-Vis-NIR range and X-ray absorption spectroscopy (XAS) together with Density Functional Theory (DFT). The electronic properties are found to be consistent with earlier reports. In order to properly account for the electron-electron correlation effects within DFT, the GGA+ U functional is employed where the appropriate value of U is obtained by comparison with the UV-Vis-NIR and O-1s XAS spectra.

Our study points out the existing knowledge gaps and highlights the subtleties regarding the structural characterization of BFN and high pseudosymmetric complex perovskites in general. The XRD pattern alone may not be sufficient to correctly characterize the structural symmetry. A combined XRD and NPD measurement for BFN strongly suggest that BFN crystallizes in a cubic structure with $Pm\bar{3}m$ space group. The local structure, as obtained by EXAFS, points to disordered BO_6 octahedra where the distortions are non-polar.

This article is organized as follows: In Sec II, we present the synthesis and experimental methods, which is followed by details of the DFT calculations employed in this study in Sec III. In Sec IV, we present our results and discuss their implications, and finally conclude in Sec V.

II. SYNTHESIS & EXPERIMENTAL METHODS

BFN ceramics were synthesized by the columbite precursor method. The precursor FeNbO_4 was synthesized by solid state reaction of reagent grade Fe_2O_3 (99.999%) and Nb_2O_5 (99.99%) by mixing them in predetermined amounts. The mixture was wet milled in acetone for a day, and calcined at 1150 °C for 5 hr. In the second stage, FeNbO_4 and BaCO_3 were mixed in stoichiometric ratio and calcined at 1200 °C for 8 hr for formation of BFN. The pellets of the calcined material were finally sintered at 1250 °C for 4 hr. After each stage of calcination and final stage sintering, the phases were confirmed with XRD taken at room temperature on Rigaku Miniflex II. The data were obtained in the range of $20^\circ \leq 2\theta \leq 80^\circ$, with a step size of 0.02° , using a Cu $K\alpha$ source (average $\lambda = 1.5418 \text{ \AA}$) with a beam current of 15 mA and at a potential of 30 kV.

The sintered pellets were crushed to form powder for the Neutron Powder diffraction (NPD) measurement. NPD was performed on PD-2 diffractometer [39] at the Dhruva reactor, Bhabha Atomic Research Center (BARC), India, using neutrons of wavelength 1.244 \AA in a temperature range of 300 K to 5 K. Rietveld refinement of the XRD & NPD data was carried out with the help of the FullProf program [40]. The background was fitted with 6-coefficients polynomials func-

tion, while the peak shapes were described by pseudo-Voigt profiles. In all the refinements, scale factor, lattice parameters, and thermal parameters were varied. Positional parameters were kept fixed since all atoms occupy special positions. In the initial stage, occupancy parameters of all the ions were kept fixed during refinement. It was possible to refine all the parameters together. In the next step, occupancy parameters were varied to ascertain the quality of the fit. No significant deviation were found, implying the robustness of the obtained structural model. Other cubic structural model suggested in earlier works were also considered which, however, led to slightly poorer fit.

The bandgap of the room temperature phase was determined from the diffuse reflectance measurements in the UV-Vis-NIR range as suggested by Davis and Mott [41]. The diffuse reflectance spectrum was obtained using a Perkin-Elmer 950 UV/Vis/NIR spectrophotometer. It was later converted to an equivalent Kubelka-Munk (KM) absorption spectrum [42, 43]:

$$F(R_\infty) = A \frac{(h\nu - E_g)^n}{h\nu}, \quad (1)$$

where, F is the Kubelka-Munk function of the relative reflectance of the sample with respect to a reference $R_\infty = R_{\text{sample}}/R_{\text{reference}}$, A is a proportionality constant, $h\nu$ is the incident photon energy and E_g is the bandgap. The values of n can be appropriately chosen to be $n = 1/2$ or 2 corresponding, respectively, to direct or indirect allowed transitions. Thus, the bandgap can be obtained by inverting the above relation (Eq. (1)) and, plotting $[F(R)h\nu]^{1/n}$ with suitable n as a function of energy. The intercept of the linear part of the spectrum near the absorption edge on the energy axis provides an estimate of the optical gap [41–43].

To further clarify the local structure of BFN, the X-ray absorption spectroscopy (XAS) techniques were used. The Fe $L_{2,3}$ -edge and O K-edge X-ray Absorption Near Edge Structure (XANES) spectra were recorded in the total electron yield (TEY) mode at the soft X-ray absorption spectroscopy beamline (BL-01) of the Indus-2 at Raja Ramanna Center for Advanced Technology (RRCAT), Indore, India. The synchrotron based XANES and Extended X-ray Absorption Fine Structure (EXAFS) studies at the Fe K-edge ($\sim 7112 \text{ eV}$) of the $\text{Ba}(\text{Fe}_{1/2}\text{Nb}_{1/2})\text{O}_3$ samples were carried out in fluorescence mode at the Energy Scanning EXAFS beamline (BL-09) at Indus-2 Synchrotron source (2.5 GeV, 100 mA) at RRCAT, which operates within the photon energy range 4-25 keV [44, 45]. The beamline optics consists of a Rh/Pt coated meridional cylindrical mirror used for the collimation of the beam. The collimated beam is subsequently monochromatized by a Si (111) ($2d = 6.2709 \text{ \AA}$) based double crystal monochromator (DCM). The pre-mirror used prior to the DCM also helps in higher harmonic rejection. Second crystal of the DCM is a sagittal cylindrical crystal, which is used for horizontal focusing of the beam while another Rh/Pt coated bendable post mirror facing down is used for vertical focusing of the beam at the sample position. For the measurement in the fluorescence mode the sample was placed at 45° to the incident beam. The fluorescence signals (I_f) were collected

using a Si drift detector placed 90° to the incident beam (45° to the surface of the sample) and the 1st ionization chamber measures the incident beam (I_0). In this way the X-ray absorption coefficient of the sample is determined by $\mu = I_f/I_0$, and the spectrum was obtained as a function of energy by scanning the monochromator over the specified range.

In order to get the oscillation in the EXAFS spectrum, the energy dependent normalized absorption coefficient $\mu(E)$ was converted to energy dependent absorption function $\chi(E)$ and then to the wave number dependent absorption coefficient $\chi(k)$. Finally, k^2 weighted $\chi(k)$ spectra were Fourier transformed in real space to generate the $\chi(E)$ versus R (or FT-EXAFS) plots in terms of the real distance from the center of the absorbing atoms. The analysis of the EXAFS data was performed following the standard procedure [46, 47] using the available IFEFFIT software package [48]. The generation of the theoretical EXAFS spectra was done using the FEFF 6.0 code. During the fitting process the EXAFS parameters *i.e.* bond distance (R) between the respective atomic pairs along a particular scattering path and the disorder factor (Debye-Waller factor σ^2) were varied independently. The FT- $k^2\chi(k)$ spectra have been fitted using the standard model obtained from the Neutron diffraction study. For the purpose of fitting, data in the k^2 weighted $\chi(k)$ spectra have been taken within the k range $2.5 - 8.5 \text{ \AA}^{-1}$ with the phase uncorrected R range $1 - 3.7 \text{ \AA}$. The goodness of the fit in the above process is generally expressed by the R_{factor} which is defined as:

$$R_{\text{factor}} = \sum \frac{[\text{Im}(\Delta\chi(r_i))]^2 + [\text{Re}(\Delta\chi(r_i))]^2}{[\text{Im}\chi_{\text{dat}}(r_i)]^2 + [\text{Re}\chi_{\text{dat}}(r_i)]^2} \quad (2)$$

where $\Delta\chi = \chi_{\text{dat}} - \chi_{\text{th}}$ is the difference between the experimental and theoretical $\chi(R)$ values and Im and Re refer to the imaginary and real parts of the respective quantities.

III. COMPUTATIONAL DETAILS

The obtained structure after the refinement of the XRD and NPD data is the perovskite $Pm\bar{3}m$ structure, which implies that the B-site cations, Fe and Nb, share the same Wyckoff position ($2a$) and are randomly occupied. Within DFT, description of “disordered” systems remains a challenge. A theoretical analysis of such a structure requires calculations with large supercells and for different possible ensembles for B-site occupancy [49]. We consider $2 \times 2 \times 2$ supercell structures with 1:1 occupation of the B-site by Fe and Nb atoms. The relative energy difference between these structures is found to be $\lesssim 0.25 \text{ eV/f.u.}$ (see Table III for details). Due to limited size of the supercell and cubic symmetry of the compound, each of the resulting structures possesses ordering of the Fe and Nb ions along different directions. Nevertheless, insights into the electronic properties of BFN can be obtained by considering the lowest energy structure among these, which is the adopted strategy here. The lowest energy configuration corresponds to an ordered arrangement of Fe and Nb ions in the Wyckoff position $2a$ along all the crystal directions, leading to a face-centered cubic $Fm\bar{3}m$ structural model. We focus

on this structure model for detailed investigations of the electronic properties.

It is important to note that, within the adopted computational scheme, although the lattice parameters are doubled (unit cell is doubled), the position of the O atoms are kept fixed at $(1/4, 0, 0)$ corresponding to the ideal face-centered cubic structure since there are no free parameters in the atomic positions of the $Pm\bar{3}m$ structure. The optimal volume obtained in the Generalized Gradient Approximation (GGA) for the $Fm\bar{3}m$ phase is approximately 4.3% larger than obtained from XRD and NPD refinements (see Fig. 9), which is a typical difference. In the following, however, we consider only the experimental lattice constant.

All calculations were carried out within the Perdew-Burke-Ernzerhof (PBE) implementation [50] of GGA using the Full-potential Augmented Plane Waves plus local orbital (FP APW+lo) method as implemented in WIEN2k 17.1 [51]. A $12 \times 12 \times 12$ k -mesh of the full Brillouin zone was used for the numerical integration together with $R_{\text{MT}} \times K_{\text{Max}} = 7.0$. An energy cut-off of -6.0 Ryd was chosen to separate the core and valence states. Electron-electron correlation effects were included via the spherically symmetric self-interaction correction (SIC) [52] double counting term of the GGA+ U functional. The self-consistency is better than 0.0001 e/a.u.^3 for the charge density and the stability is better than 0.01 mRy for the total energy per unit cell. For comparison with the O K-edge XAS spectra, a constrained calculation was also carried out with a core-hole in only one of the O-1s states in the unit cell.

IV. RESULTS & DISCUSSIONS

A. Structural Properties

We begin with an overview of the reported crystal structures of BFN ceramics. The most commonly employed synthesis technique is the solid-state reaction method, which may [32, 34, 36, 53–55] or may not [19–24, 26, 37, 38] involve the use of a B-site precursor. Additionally, conventional ceramic method [18, 31], powder calcination [17], sol-gel method [35], chemical synthesis [29], mechanical triggering [56], and mechanochemical [57] routes have also been employed. The reported structural data comprises of perovskite cubic $Pm\bar{3}m$ structure, double perovskite cubic $Fm\bar{3}m$ as well as monoclinic structures. However, any correlation between the choice of synthesis method or synthesis parameters and the resulting structure could not be established. For brevity, we tabulate the synthesis method, synthesis parameters and the resulting crystal structures in Table V (Appendix E).

Even within the standard solid-state reaction techniques (without the involvement of a precursor), both cubic and monoclinic structures have been reported. The earliest work by Yokosuka in 1995 reported a cubic perovskite $Pm\bar{3}m$ structure [19]. However, in 2002, Saha and Sinha reported a monoclinic structure [20]. The two methods differ in values of calcination and sintering temperatures used during the synthesis. However, subsequent works using similar calcination

temperatures as used by Saha and Sinha have reported either cubic $Fm\bar{3}m$ [21, 24], or monoclinic [28, 33] or cubic $Pm\bar{3}m$ structures [23, 27, 31]. With regard to the calcination temperature, it is found that temperature above 900° is required for the formation of BFN samples [23]. However, this doesn't influence the resulting structural symmetry and all the reported studies meet this requirement. Similarly, the sintering temperature influences only the quality of the resulting sample, it has no effect on the crystal structure [32].

The use of a B-site precursor has been proposed as an effective method to obtain high quality samples in Pb-based perovskites, for example the Pb-counterpart, $Pb(Fe_{1/2}Nb_{1/2})O_3$ (PFN) [58]. In both PFN and BFN, the columbite precursor $FeNbO_4$ is used, which crystallizes in a monoclinic (wolframite $P2/c$ or $AlNbO_4$ -type $C2/m$), orthorhombic (ixiolite $Pbcn$), or tetragonal (rutile $P4_2/mnm$) structure. Among these, the use of monoclinic wolframite structure and the orthorhombic rutile structures have received some attention. For BFN, a comparison between the samples synthesised using the columbite precursor and direct mixing of initial compounds (oxides and carbonates) suggests that columbite precursor methods should be the method of choice for technological applications since it leads to low dielectric loss [32].

During the synthesis of BFN using the columbite precursor, Ke *et al.* [32, 53, 54] have carefully chosen the monoclinic precursor (calcination temperature of 1075° for the precursors) as if the structural symmetry of the precursor and the resulting BFN samples are correlated. While they find the resulting BFN ceramics possessing monoclinic structure, this causal relationship has never been established. In fact, for the related PFN ceramics, it was explicitly shown that the structural symmetry of the precursor does not play any role in the structure of resulting ceramics [58].

Other works which use similar calcination temperature for the precursor have found either a monoclinic [36] or a cubic $Pm\bar{3}m$ structure [55]. The difference in the structural symmetry could be due to different choice of calcination temperature during the second-stage mixing of the precursor with the $BaCO_3$. The higher calcination temperature during this stage led to a $Pm\bar{3}m$ structure. However, this apparent dependence of the crystal structure of BFN on the crystal structure of the precursor is in sharp contrast to PFN, and possibly misleading.

A closer inspection of the available XRD patterns for different reported crystal structures irrespective of the synthesis route, reveals that the source of such discrepancy could be related to high pseudosymmetry of the perovskite BFN ceramics. The XRD patterns presented in Ref. [19] for $Pm\bar{3}m$, Ref. [20] for monoclinic, and Ref. [18] for $Fm\bar{3}m$ structures are almost identical. In fact, such conflicting structural characterization is of concern and has remained a challenge for a long time [59]; one of the notable example in recent times being the Van Vleck paramagnet Sr_2YIrO_6 [60, 61].

For compounds with possible high pseudosymmetry, the characterization should be based on a careful analysis of the presence of additional reflection peaks and/or peak splittings. It is interesting to note that among all the claims for monoclinic structure, such an evidence for a monoclinic structure is available only in Ref. [62], where the XRD data shows

clear peak splitting of the (220) and (222) reflection peaks. However, such splitting of the (220) reflection peak is absent in other claims. Moreover, some of the authors in Ref. [62] have also claimed cubic structures based on similar synthesis parameters. Arguably, the realization of the monoclinic structure is possibly due to some experimental factors other than the calcination and sintering temperatures used. We, therefore, consider this as an outlier. (This data has also been omitted from Table V.)

Empirically, tolerance factor, defined as:

$$t = \frac{r_A + r_O}{\sqrt{2}(\bar{r}_{B,B'} + r_O)}, \quad (3)$$

can be a useful guide to ascertain if the resulting structure could be cubic [42, 63]. Here, r_A , r_O , and $\bar{r}_{B,B'}$ are the ionic radii of the A-site cation, O ion and average of the B-site cations, respectively. $t = 1$ represents the ideal case of a cubic unit cell with perfect matching between the A- and B-site ionic radii. Therefore, if $t \approx 1$, a cubic structure is expected. For $t < 1$, the size mismatch between the radii of the A- and B-sites leads to octahedral distortions, lowering the symmetry to orthorhombic, tetragonal or monoclinic structures. If $t > 1$, the A-site ion is too big (compared to the B-site cations), leading to distortion of the structure towards a hexagonal or tetragonal symmetry. Note, however, that the accuracy of this method is approximately 83% for perovskite oxides.[63] For BFN, it turns out that $t = 1.04$, suggesting that a cubic structure is possible. The degree of cation ordering is determined by the ratio of ionic radii of the B-site cations, large difference usually leads to long range cation ordering. By the fact that both the B-site cations Fe^{3+} and Nb^{5+} have nearly the same ionic radii, a large degree of cation disordering is expected.

A possible way to clarify the structural details (especially cation ordering and atomic parameters) is to perform a careful analysis of simultaneous XRD and NPD measurements since they provide complementary information. The cubic and monoclinic crystal symmetries lead to distinct reflection peaks (*e.g.* splitting of the (220) peak only for monoclinic unit cells) and can be distinguished by a high resolution XRD as well as NPD data. On the other hand, as NPD is more sensitive to the positions of O atoms,[59] the oxygen position can be accurately determined in the NPD data, which differ in the cubic $Pm\bar{3}m$ and $Fm\bar{3}m$ symmetries, as discussed below. This is precisely the strategy employed in this work.

Our choice of the synthesis parameters is same as in Ref. [32], except for the calcination temperature during the preparation of the precursor (see Sec. II). We checked that this does not affect the structural symmetry of the precursor, which was found to be monoclinic (see App. A for details).

Figures 1(a) & (b), respectively, show the XRD and NPD patterns for the synthesized BFN samples at room temperature. The Rietveld refinement of the XRD and the NPD data reveals that BFN crystallizes in the cubic $Pm\bar{3}m$ (No. 221) structure at ambient temperatures. In the XRD data, the (220) peak at $2\theta \sim 65^\circ$ is not split [shown in the inset of Fig. 1(a)], confirming the cubic structure. Similarly, no superlattice reflection peaks corresponding to a monoclinic structure were observed in the NPD data either.

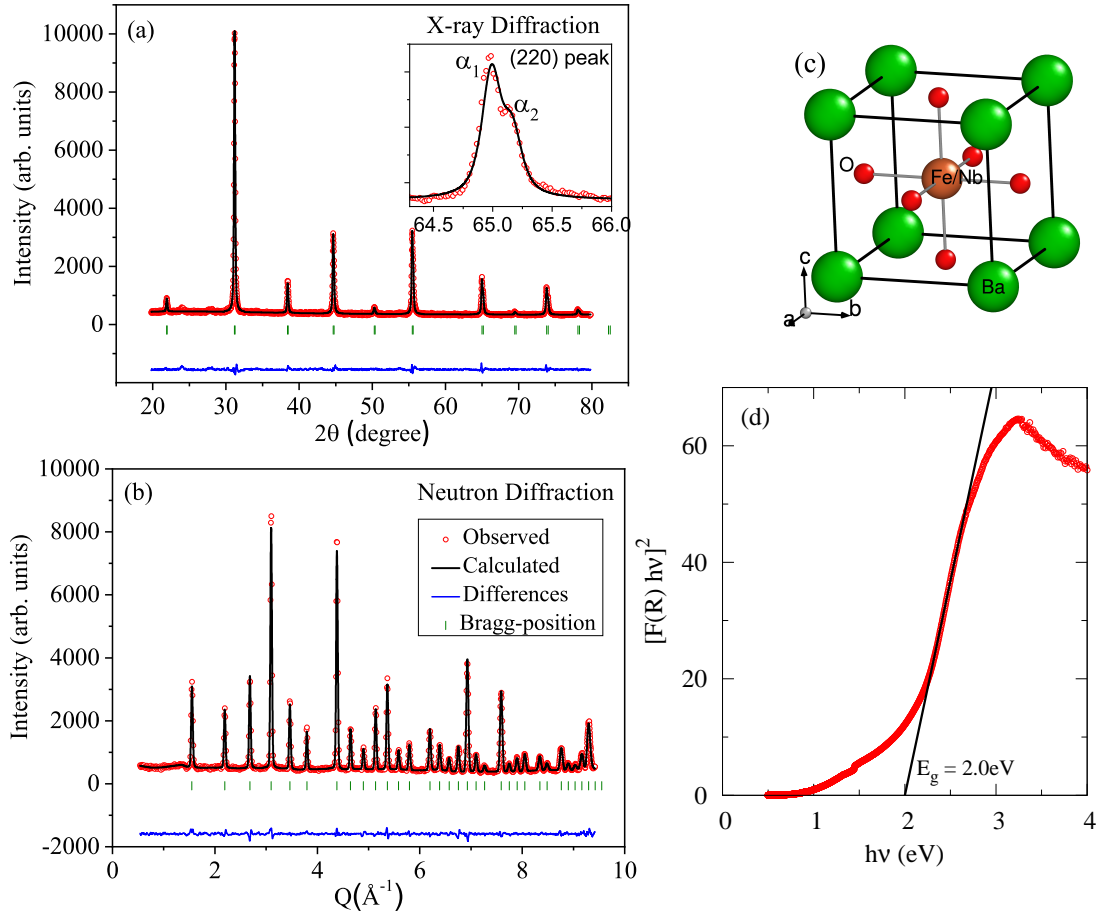


FIG. 1. Room temperature (a) XRD data, (b) NPD Data and (c) the resulting crystal structure of BFN. The inset in (a) shows the non-split (220) peak confirming the cubic structure. The doublet α_1 and α_2 corresponds to the Cu $K\alpha_1$ and $K\alpha_2$ beams. (d) Kubelka-Munk function vs energy showing a direct bandgap of approximately 2eV.

TABLE I. Structural parameters obtained from NPD measurements.

A. Refinement parameters			
Param	300 K (ND)	5 K (ND)	
Space group	$Pm\bar{3}m$ (No. 221)	$Pm\bar{3}m$ (No. 221)	
$a = b = c$ (Å)	4.0556(2)	4.0466(1)	
$\alpha = \beta = \gamma$	90°	90°	
Final R-indices:			
R_p	3.94	3.92	
R_{wp}	5.02	5.10	
R_{exp}	3.69	3.68	
Goodness of Fit (GoF)	1.85	1.91	
B. Structural parameters at 300 K from neutron diffraction			
Atom	Position	Occupancy	B_{iso} 300K & 5K
Ba	(0,0,0)	1.0	0.58(4) & 0.22(3)
Fe	(1/2,1/2,1/2)	0.50	0.59(4) & 0.35(3)
Nb	(1/2,1/2,1/2)	0.50	0.59(4) & 0.35(3)
O	(1/2,1/2,0)	1.0	0.68(3) & 0.39(3)

The distinction between the cubic $Pm\bar{3}m$ and $Fm\bar{3}m$ structures arises from long range cation ordering in the B-site, leading to different sizes of the BO_6 (and $B'O_6$) octahedra. The $Fm\bar{3}m$ structure corresponds not only to a doubled cell but

the position of the oxygen atom (x coordinate) is also a variable (Wyckoff site $24e$). Depending on the ionic radii, electronegativity, and hybridization with oxygen for the transition metal cation, the B-O and B'-O bonds are of different length.

In comparison, in the $Pm\bar{3}m$ structure, the oxygen coordinate is fixed at the center of the B/B' positions. As the oxygen atom scattering has more information content in NPD patterns compared to XRD patterns, it is possible to decipher the position of the oxygen atoms, and thus, also the appropriate structural model. Any deviation of oxygen atom x -coordinate in the $Fm\bar{3}m$ structure should lead to non-zero intensities in the super lattice reflections. It should be noted that, in the investigated samples, both the structural models fit the data well (based on the goodness of fit). However, we find that all the super lattice reflections in $Fm\bar{3}m$ model fit have zero intensity (see Appendix B). Consequently, the oxygen positions are such that the (average) size of the BO_6 and $B'O_6$ octahedra are identical despite different electronegativities of the B and B' cations, thus, leading to the $Pm\bar{3}m$ structure model. Similarly, monoclinic phase can also be ruled out as any other superlattice reflection other than for perovskite cubic $Pm\bar{3}m$ in NPD and cubic symmetry in XRD was not observed. Moreover, no signature of any subtle structural transition was observed based on the analysis of the full-width half-maxima (FWHM) of the Bragg peaks in the NPD data at 300 K and at 5 K (see Appendix B). Therefore, based on a combined XRD and NPD data analysis, we unambiguously establish the structure of $Ba(Fe_{1/2}Nb_{1/2})O_3$ ceramics to be cubic $Pm\bar{3}m$.

From the NPD data refinement, the lattice constant was found to be 4.0556 Å at 300 K and the chemical formula matches with that of a single perovskite $Ba(Fe_{0.5}Nb_{0.5})O_3$ as reported in some of the previous studies. Also, no structural transition was observed down to 5 K. The structural details are presented in Table I and the corresponding crystal structure is shown in Fig. 1(c).

B. Optical bandgap (UV-Vis)

Figure 1(d) shows the KM absorption spectrum as a function of the incident photon energy for $n = 1/2$ corresponding to the direct allowed transition. The gap is estimated to be approximately 2.0 eV as obtained from the intercept of the linear part on the energy axis. It is important to note that, for $n = 2$ (indirect allowed transitions), lower estimated gaps could be obtained. However, they are not in agreement with the dark brown color of the sample. On the other hand, a gap value of 2.0 eV is consistent with the sample color. Therefore, in the following, we consider the gap value of 2.0 eV to be the likely bandgap of the synthesized BFN samples.

C. Electronic Properties

1. XAS and XANES

The valency of constituent atoms can also be analyzed using X-ray absorption spectroscopy (XAS). XAS has additional advantages since it is not only elemental selective in analyzing the electronic (valence) states but also capable of probing the local structures simultaneously through X-ray absorption near edge structure (XANES) and extended X-ray ab-

sorption near edge structure (EXAFS). Fig. 2(a) shows the XANES spectra of the BFN sample measured at Fe K-edge along with that of Fe metal foil and Fe_2O_3 powder. The absorption edge lies at approximately ~ 7128 eV for BFN and ~ 7123.5 eV for the reference material Fe_2O_3 . The appearances of features just below the absorption edge is usually referred to as 'white lines' [64] and corresponds to electronic (atomic-like) transitions from the core $1s$ state into a quasi-bound state with $3d$ character. While such transitions are forbidden within the electric dipole approximation for an ideal octahedral crystal field environment, slight distortions in the MO_6 ($M = Fe, Nb$) octahedra may lead to such pre-edge feature. The pre-edge features at ~ 7115 eV are due to the $1s$ transition into unoccupied O- $2p$ - M- $3d/4sp$ hybridized states, which have p -component projected at the sites as observed in many transition metal oxides. Presence of such hybridized states with mixed pd character near the band edges is also seen in the DFT calculations (see Fig. 3(a)), as discussed in detail later.

After the pre-edge background (7115 eV) subtraction, the spectra are normalized to unity, averaging the signal between the edge jumps and about 50 eV above the white line. We also measure the spectra for Fe metal foil as reference. It is evident from a comparison between these spectra that the Fe K-edge in the sample lies slightly above that of Fe_2O_3 , implying that the oxidation state of Fe in the present sample is $+3$.

The intensity and peak position of the pre-edge depends critically on the local structure and the oxidation state [65]. Since the Fe ions in Fe_2O_3 are known to be highly non-centrosymmetric, the fact that the intensity of the pre-edge for BFN is much weaker than that for Fe_2O_3 is indicative of the fact that the off-center displacement of Fe ions is negligible. This is further substantiated by the fact the peak lies at somewhat higher energy than for Fe_2O_3 , similar to the primary absorption peak, and that the primary absorption (dominant) peak is much steeper. These findings essentially rule out any non-centrosymmetric position of the Fe^{3+} ions and are consistent with an ideal $Pm\bar{3}m$ structural characterization [65].

For the L-edge shown in Fig. 2(b), the possible transitions from $2p_{1/2}$ and $2p_{3/2}$ states to the d states lead to L_2 and L_3 peaks in the XAS spectra. These peaks further split into two peaks which is a characteristic at the $L_{2,3}$ edge of all d^n compounds in an octahedral or tetrahedral environment due to transitions to t_{2g} and e_g levels. This ligand field splitting is estimated to be ~ 1.5 eV. The spectrum is very similar to Fe_2O_3 as would be expected for Fe^{3+} ions.

Figure 2(c) shows the normalized XAS for the O K-edge of BFN. The low-energy part of the XAS spectrum is dominated by the energy positions of the TM- d states due to the strong covalent bonding among the transition metal TM- d and O- $2p$ orbitals. The low-energy features lying at ~ 526.5 eV and ~ 531.6 eV should be related to the low energy transition from O- $1s$ state to the O- $2p$ states hybridized with the d -states from the transition metals Fe and Nb. These features are also confirmed by the first principles calculations and will be used to obtain a reliable estimate of the strength of U for GGA+ U calculations, as discussed in the following. The features at en-

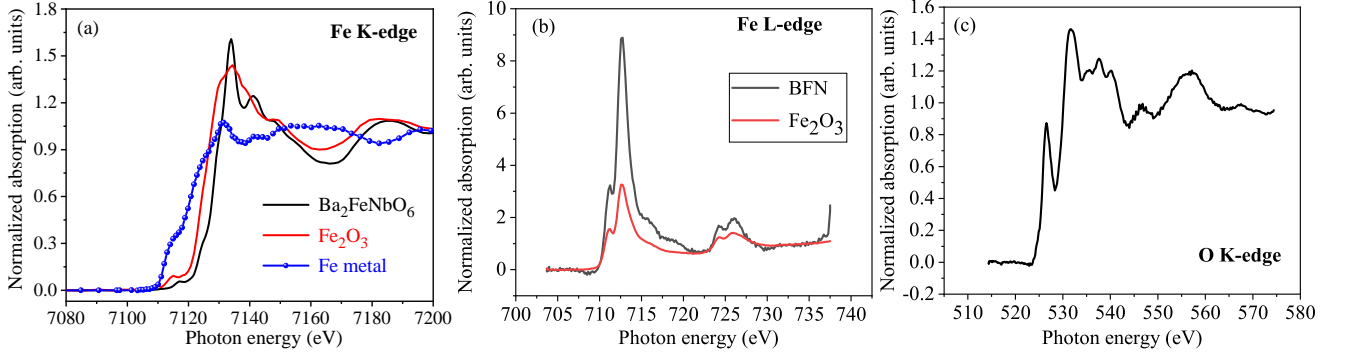


FIG. 2. (a) Normalized XANES spectra at Fe K-edge compared to reference material Fe_2O_3 and Fe metal, and (b) XAS for Fe L-edge in BFN and Fe_2O_3 . (c) XAS spectrum for the O K-edge in BFN. See text for further details.

ergies greater than ~ 536 eV can be attributed to transitions to the higher lying hybridized O- $2p$ – TM- sp states. These findings are consistent with the DFT calculations.

2. DFT

The total and partial density of states (DOS) within GGA ($U = 0$) is shown in Fig. 3. The states across the Fermi energy are largely composed of Fe- $3d$ states. Due to the octahedral ligand field exerted by the O atoms, the d -shell splits into t_{2g} and e_g levels, t_{2g} being lower in energy. For the up-spin channel, the t_{2g} and e_g states lie between the Fermi energy ε_F and -6 eV. In the down spin channel, the ligand field is estimated to be approximately 1.5 eV, which is in agreement with the corresponding value estimated for XAS (see Fig. 2(b)). Consistent with the formal valency of +3, the Fe- d states are half-filled (fully populated by up-spins) and, therefore, experience large exchange splitting of approximately 2.7 eV (4.0 eV) in the e_g (t_{2g}) sub-bands. The Nb atoms, on the other hand, possess an empty d -shell, consistent with the formal valency of +5. The octahedral ligand field environment also splits these states into t_{2g} and e_g levels which lie at approximately 2.6 eV and 7 eV, respectively, corresponding to a ligand field splitting of approximately 4.5 eV. The much larger CF splitting of the Nb- $4d$ states compared to Fe- $3d$ can be understood by the larger spatial extension of the former. However, the exchange splitting is negligible. The magnetic moment on the Fe atoms is found to $\sim 5\mu_B$, consistent with the d^5 occupation.

The ground state within GGA is found to be gapless (semi-metallic) in sharp contrast to the diffuse reflectance measurements (UV-Vis-NIR spectra). This is not too surprising for the applied GGA. Fig. 3(b) shows the GGA band structure. It is interesting to note that the spin-resolved band structure has an indirect gap for the up-spin between the high symmetry points L ($\pi/a, \pi/a, \pi/a$) and X ($0, 2\pi/a, 0$).

The electron-electron correlations beyond GGA are accounted for via GGA+ U calculations. Since the Nb- d states are unoccupied, it may suffice to only apply $U_{\text{eff}} = U - J$ (with $J = 0$) to the Fe- $3d$ shell. With U , a gap opens and increases

with increasing values of U (see D for more details). Figs. 3(c)-(f) show the evolution of DOS with U . With increasing values of U , the unoccupied Fe $d - t_{2g}$ (occupied Fe $d - e_g$) states shift higher (lower) in energy. The Nb- d states, however, remain unaffected. For the entire range of considered U -values, the ground state corresponds to a half-filled Fe- d shell, with a net spin moment of approximately $5\mu_B$ per Fe atom as was the case for $U = 0$.

For $U \sim 6 - 7$ eV, the bandgap is approximately 2 eV in agreement with the value obtained from the diffuse reflectance measurement. However, it is important to note that the gap remains indirect for all values of U up to 7.5 eV and corresponds to a spin-flip electronic transition (possibly assisted by phonons). The origin of such a discrepancy is likely due to the fact that the DFT calculations are performed for the $Fm\bar{3}m$ structures with an ordered occupation of the B-sites by Fe and Nb atoms whereas the NPD data suggest a “disordered” arrangement of B-site cations. Therefore, it is instructive to carry out a detailed investigation of possible structures with random occupation of B-site cations by considering larger supercells [49], which is beyond the scope of the present work.

In order to tune the estimate of U for BFN, we compare the DFT results with the XAS spectra. Specifically, we compare the position of TM- d states in the conduction band for several values of U with the low-energy part of the O K-edge spectra. We find that, indeed, the experimental XAS spectrum is well explained by considering $U = 6$ eV for Fe- $3d$ states. Fig. 4 shows a comparison between the experimental and simulated spectra. The low-energy peak positions are identified by performing a multiple-peak (Gaussian) fitting of the experimental curve. The peak positions in the simulated (theoretical) spectra compare well with the experimental values. Consideration of core hole in the O- $1s$ state influences the relative intensity of these low-energy peaks and leads to an improved agreement with the experimental data. Looking at the partial DOS for the TM- d states (Fig 3), it is clear that the low energy peak at approximately 527 eV is due to hybridized states from both Fe- d and Nb- d with O- $2p$, whereas the peak at approximately 532 eV is largely due to hybridization between O- $2p$ and Nb- e_g states. With regard to the values

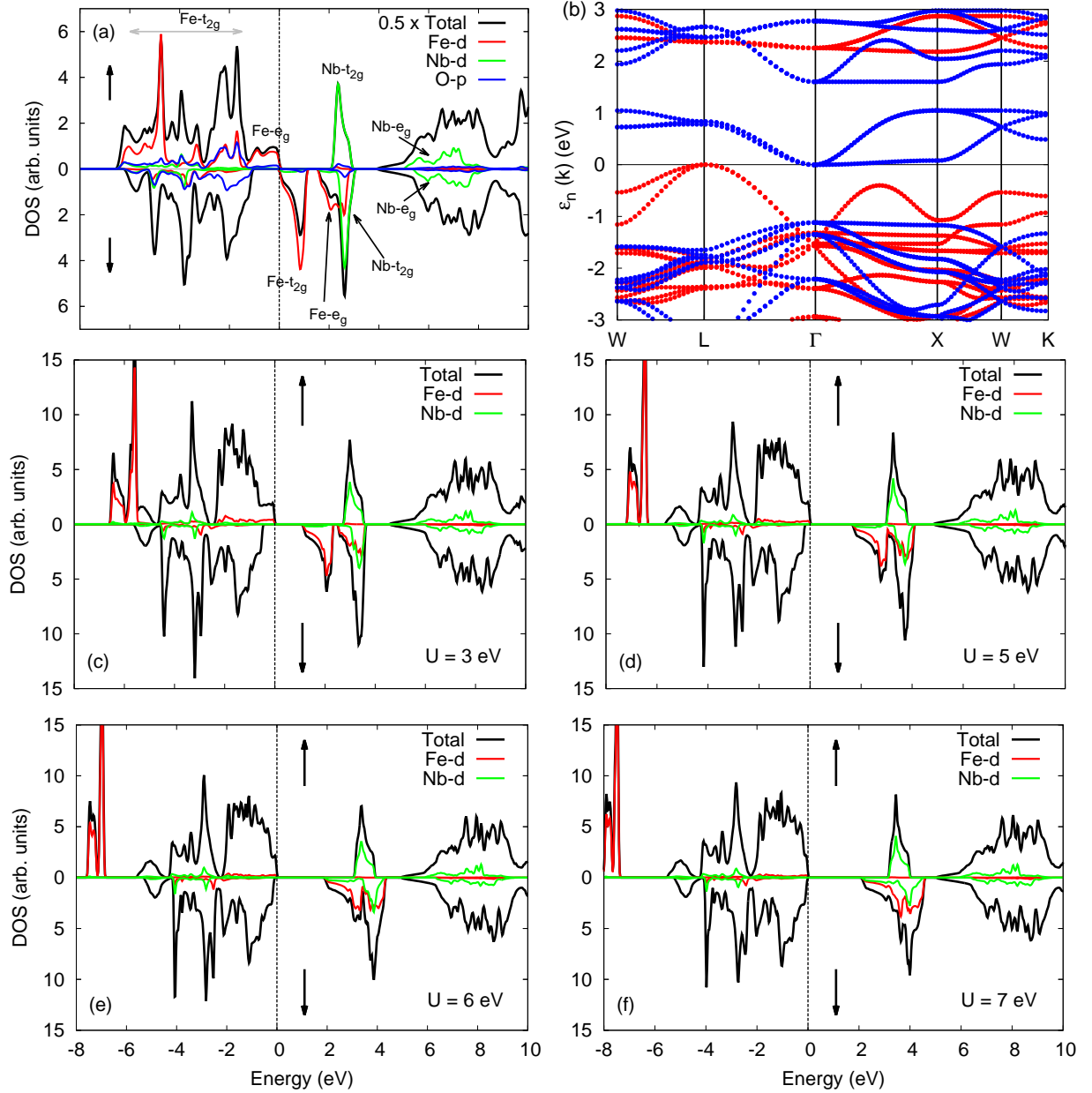


FIG. 3. The electronic properties of BFN: (a) spin-projected total and (atom-resolved) partial density of states (DOS) obtained within GGA scalar relativistic calculations ($U = 0$). The spin components are represented by up and down arrows. The corresponding band structure is shown in (b), where spin up (down) bands are shown in red (blue). The high-symmetry points are located at: W ($\pi/a, 2\pi/a, 0$), L ($\pi/a, 2\pi/a, \pi/a$), Γ (0,0,0), X ($0, 2\pi/a, 0$) and K ($3\pi/2a, 3\pi/2a, 0$). (c)-(f) The evolution of the total and TM-d partial DOS with U . The Fermi energy is set to $\epsilon_F = 0$.

of U , a similar value for Fe-d states was also suggested for a related compound $\text{Pb}(\text{Fe}_{1/2}\text{Ta}_{1/2})\text{O}_3$ [66].

3. EXAFS

To probe the local structural aspects of the BFN sample, we carried out EXAFS studies [65]. Fig. 5(a) shows the Fe K-edge EXAFS spectra ($\mu(E)$ vs. E data) of the sample, from

which the equivalent absorption function $\chi(k)$ was obtained. Fig. 5(b) shows the k^2 weighted $\chi(k)$ vs. k plot, and the $\chi(R)$ versus R plot is shown in Fig. 5(c). In the $\chi(R)$ versus R plot, there are three well-defined peaks lying between 1 Å and 4 Å. The peak around 1.5 Å corresponds to the Fe-O bond length. This peak contains information regarding the off-center displacement of Fe ions and distortions of the FeO_6 octahedra. It is interesting to note that there is only one well-defined and reasonably sharp peak, confirming the negligible

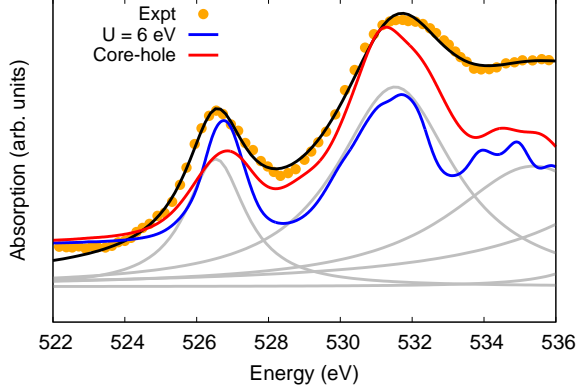


FIG. 4. Comparison of the theoretical and experimental XAS O K-edge spectra. A fit of the peak positions in the experimental spectrum using Lorentzian functions is shown in gray solid curves. The resultant curve is shown with black solid line. The theoretical spectra was obtained with (red solid curve) and without (blue solid curve) considering core hole in the O-1s state, for $U_{\text{eff}} = 6$ eV.

TABLE II. EXAFS best fitted parameter values. The bond length values in brackets correspond to the structure obtained from the NPD data.

Parameters		BFN
Scattering Path	S_0^2	0.85
\times C.N.	E_0 (eV)	-5.976 ± 0.40
Fe–O $\times 6$	R (Å)	2.00 ± 0.01
(2.023 Å)	σ^2 (Å ²)	0.014 ± 0.001
Fe–Ba $\times 8$	R (Å)	3.41 ± 0.02
(3.504 Å)	σ^2 (Å ²)	0.025 ± 0.004
Fe–Nb/Fe $\times 6$	R (Å)	3.77 ± 0.01
(4.047 Å)	σ^2 (Å ²)	0.003 ± 0.001
R_{factor}		0.012

off-center (non-centrosymmetric) displacement of the Fe ions [65]. The peak around 3.5 Å can be attributed to the interatomic distance between the B-site cations (Fe-Fe or Fe-Nb distances).

We have also theoretically simulated these features assuming the structure of the sample obtained from the NPD measurements. The comparison between the simulated and experimental spectra along with the corresponding interatomic distances are also shown in Fig 5(c). Evidently, the qualitative and the quantitative agreement between the two curves is very good in the range of 1 – 3.7 Å. The corresponding best fit results of the fitting parameters (R and σ^2) are shown in Table II.

Our primary interest is in the Fe-O distance since this contains information regarding the local structure. We find that the theoretical estimate of 2.0 Å is in a very good agreement with the experimental XRD/NPD value. The Fe-Ba and Fe-Nb distances however show deviations of approximately

0.1 Å and 0.3 Å. The peak corresponding to the interatomic distance between the B-site cations in perovskites materials is sensitive not only to their distance but also to the bond angle TM-O-TM (TM=Fe/Nb). Deviation between the theoretical and experimental estimates is likely caused by the relative difference in electronegativity and oxidation state of the two ions and is indicative of the fact that the BO_6 and $\text{B}'\text{O}_6$ octahedra are slightly distorted. Nevertheless, the average Fe-O distances turn out to be in good agreement with the expected value, implying that these distortions are non-polar in nature. Therefore, the local structure, especially the distances between transition metals as well as with oxygen, obtained via EXAFS is in an excellent agreement with the crystal structure determined by NPD.

V. CONCLUSIONS

In summary, we have carried out an in-depth study of the structural and electronic properties of the BFN ceramics. Combined XRD, NPD and EXAFS studies put to rest the existing discrepancies related to the structural details of this material. The study reveals a cubic $Pm\bar{3}m$ structure ($a = 4.0556$ Å at 300 K) with the chemical formula corresponding to the perovskite $\text{Ba}(\text{Fe}_{1/2}\text{Nb}_{1/2})\text{O}_3$.

More importantly, the presented analysis of the available structural reports highlights subtleties in structural characterization of complex perovskites with high pseudosymmetry. In such cases, it may be particularly challenging to correctly characterize the structural symmetry and, therefore, complementary techniques should be employed. Combined XRD and NPD measurements together with a careful analysis of the data provide such a framework.

Regarding the electronic properties, a good agreement is found between XAS and DFT studies. The formal valency of B-site transition metals Fe and Nb is found to be +3 and +5, respectively. Consequently, the Fe-3d is half-filled with spin up electrons while the Nb-4d states are unfilled, leading to a net spin moment of $5 \mu_B$ on each Fe atom. The ground state is insulating. The gap is estimated from the diffuse reflectance measurement in the UV-Vis-NIR range and the estimated gap of approximately 2.0 eV is consistent with the sample color.

From a theoretical standpoint, DFT calculations for an $Fm\bar{3}m$ structure model (considering a $2 \times 2 \times 2$ supercell) within GGA provides a good qualitative and quantitative description of the electronic properties. A rather large value of $U_{\text{eff}} \sim 6$ eV is needed to account for the correlation effects. However, it turns out that the nature of bandgap is inconsistent with the experimental results and larger supercells must be considered to account for the random B-site occupation and/or distortion in the BO_6 octahedra.

Note added: During the preparation of the manuscript, we became aware of a recent study which also reported a cubic $Pm\bar{3}m$ structure using high resolution synchrotron X-ray powder diffraction (SXRPD) measurement. [67]

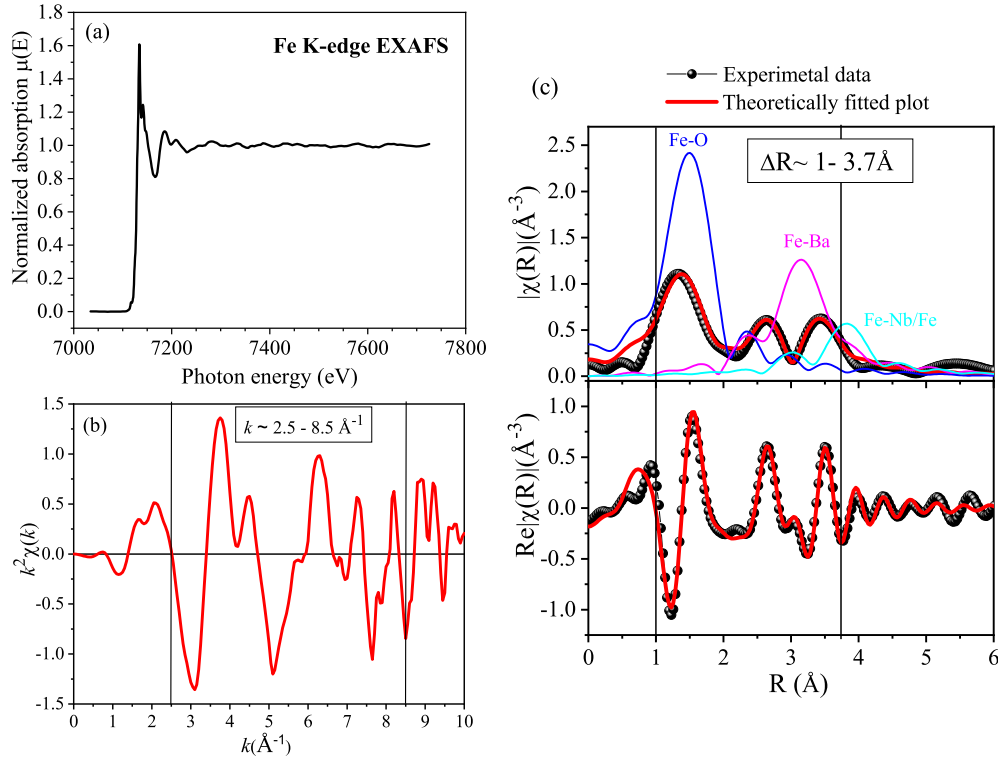


FIG. 5. (a) Normalized EXAFS spectrum at the Fe K-edge. (b) k^2 weighted $\chi(k)$ spectra at Fe K-edge, and (c) the theoretically generated model (red line) with contributions for atomic pairs: Fe-O (blue), Fe-Ba (pink) and Fe-Nb/Fe (cyan).

ADDITIONAL INFORMATION

Competing interests. The authors have no conflicts to disclose.

ACKNOWLEDGMENTS

We thank Dr. Kaustava Bhattacharya, Dr. Steffen Oswald, Dr. B. K. Singh, and Dr. Sai Aswartham for helpful discussions. RR thanks Ulrike Nitzsche, Valligatla Sreeramulu and V.V. Aneesh for technical support. RR and MR acknowledge financial support from the European Union (ERDF) and the Free State of Saxony via the ESF project 100339533 (Young Investigators Group Computer Simulations for Materials Design –CoSiMa) during the initial part of the project.

DATA AVAILABILITY STATEMENT

The data that support the findings of this study are available from the corresponding author upon reasonable request.

Appendix A: Structural characterization of FeNbO₄

Figure 6 shows the XRD pattern of the precursor composed of FeNbO₄ and Fe₂O₃. The corresponding Rietveld refinement suggests a monoclinic structure for FeNbO₄.

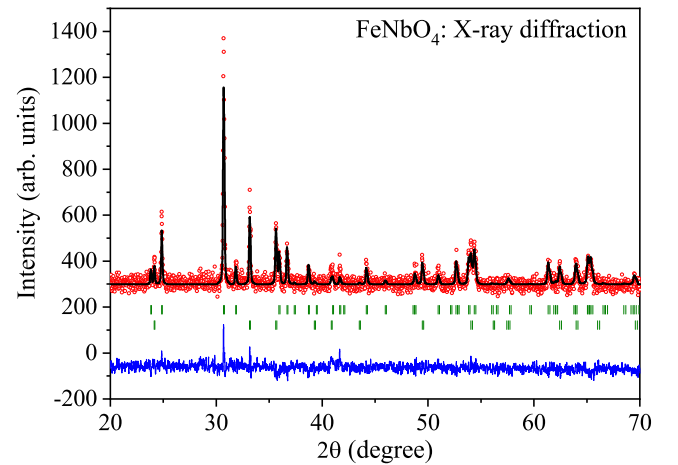


FIG. 6. XRD pattern and Rietveld refinement of the precursor. The Bragg positions are shown with the vertical bars for both FeNbO₄ (top) and Fe₂O₃ (bottom). The crystal structure of FeNbO₄ is identified to be the monoclinic $P2_1/c$ structure.

Appendix B: Analysis of the NPD data for other structural models

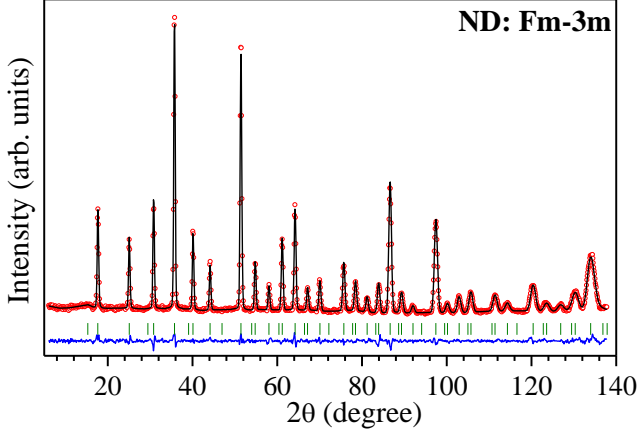


FIG. 7. Fit of the room temperature NPD data to the $Fm\bar{3}m$ structural model.

Figure 7 shows the fit of the $Fm\bar{3}m$ structural model to the NPD data. The final R-indices for the fit to the $Fm\bar{3}m$ structure are: $R_p = 3.94$, $R_{wp} = 5.02$, and $R_{exp} = 3.70$, and the GoF = 1.92. Therefore, the quality of the fit is comparable to the $Pm\bar{3}m$ structural model (see Table I). However, despite the quality of the fit, any sublattice reflection peaks corresponding to deviation of the oxygen position from the center of the Fe/Nb positions are absent, ruling this out as an appropriate structural model for the synthesized BFN ceramics.

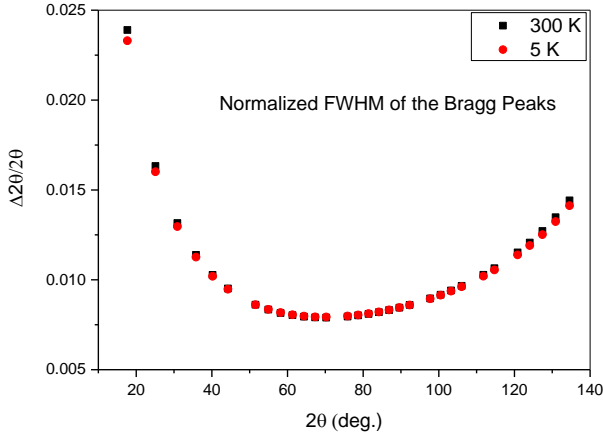


FIG. 8. Normalized FWHM of the Bragg peaks of the NPD data at 300 K and 5 K, showing absence of structural distortion.

Similarly, no superlattice reflection peaks were observed for the monoclinic structure. To investigate any subtle structural transformation at low temperature, we study the full-width half-maxima (FWHM) of the Bragg peaks in the NPD data as well. Figure 8 shows that the FWHM does not change between 300 K and 5 K, thus ruling out structural transitions.

Appendix C: Considered structures for DFT calculations

Table III presents the structural characteristics and relative spin-polarized GGA energies of various possible structures in a $(2 \times 2 \times 2)$ supercell. The supercell structure contains four Fe atoms and four Nb atoms. Due to the size of the supercell, all the resulting structures consist of a periodic arrangement of the TM ions:

- **S1:** alternating layers of Nb and Fe atoms along a principle direction,
- **S2:** alternating Nb and Fe atoms along all principle directions (leading to a face centered cubic structure),
- **S3:** alternating Nb and Fe atoms along a face diagonal.
- **S4:** alternating Nb and Fe atoms along a face diagonal and the principle direction orthonormal to it.

Considering the $Pm\bar{3}m$ structure obtained by XRD and NPD data, the position of the oxygen atom was kept fixed. For example, for the cubic $Fm\bar{3}m$ structure (**S3**), the position of O atoms were fixed at $(1/4, 0, 0)$.

TABLE III. Relative energies of various considered structures for $Ba(Fe_{1/2}Nb_{1/2})O_3$ obtained by considering supercells. The corresponding lattice parameters are also listed with respect to the lattice parameter obtained from NPD refinement $a = 4.0556 \text{ \AA}$.

Case	Space group	Lattice params	Energy/f.u. (eV)
S1	$P4/mmm$	$(a, a, 2a)$	0.223
S2	$Fm\bar{3}m$	$(2a, 2a, 2a)$	0.0
S3	$P4/mmm$	$(\sqrt{2}a, \sqrt{2}a, a)$	0.071
S4	$P4/mmm$	$(2a, 2a, 2a)$	0.088

The face-centered cubic $Fm\bar{3}m$ structure turns out to have the lowest energy and was used for a detailed analysis of the electronic properties. We also obtained the optimal lattice parameters for the $Fm\bar{3}m$ structure. Fig. 9 shows the dependence of energy on volume of the unit cell, as obtained within the spin-polarized GGA calculations and accounting for scalar relativistic corrections.

Appendix D: Evolution of gap with U

Table IV shows the evolution of the spin-resolved and net bandgap with U .

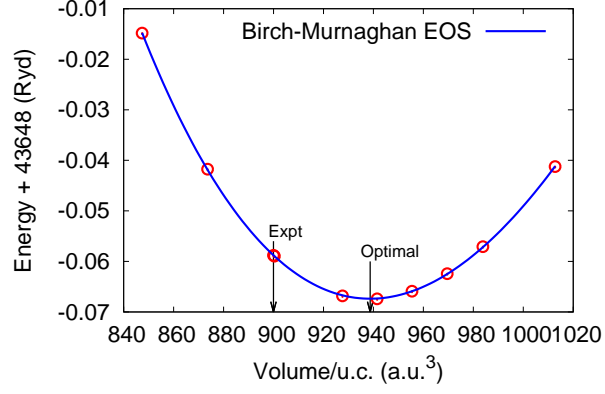


FIG. 9. Energy vs volume for the $Fm\bar{3}m$ representation of BFN, with oxygen position fixed. The open circles are the different considered volumes while the solid curve is the fitted Birch-Murnaghan equation of state (EOS). The optimal unit cell volume is 938.66 a.u.³, which is approximately 4.3% larger than the experimental value. Correspondingly the lattice constants are approximately 1.4% larger.

TABLE IV. Electronic bandgap as a function of U .

U -value (eV)	Gap (eV)		
	\uparrow -spin	\downarrow -spin	Net
0	1.07	0	0
1.0	2.38	1.27	0.40
3.0	2.75	1.58	1.09
5.0	2.99	1.87	1.65
6.0	3.10	2.01	1.89
6.5	3.13	2.07	1.99
7.0	3.15	2.13	2.10
7.5	3.18	2.19	2.19

Appendix E: Review of reported structures and synthesis parameters

TABLE V: Review of reported crystal structures for BFN ceramics along with the method and synthesis parameters. T_{cal} and T_{sin} , respectively, represent the calcination and sintering temperatures. The values in brackets are the duration; empty brackets indicate that the values are not known.

Method	Synthesis parameters		Crystal symmetry	Source
	T_{cal} [$^{\circ}\text{C}$] (duration)	T_{sin} [$^{\circ}\text{C}$] (duration)		
Solid state method (without precursor)	900 (2h)	1350 (4h)	cubic $Pm\bar{3}m$	Yokosuka <i>et al.</i> (1995) [19]
	900 (2h)	1200 (60h) \rightarrow 1300 (12h)	cubic $Fm\bar{3}m$	Tezuka <i>et al.</i> (2000) [18]
	1200 (10h)	1250 (5h)	monoclinic	Saha & Sinha (2002)[20]
	997 - 1097 (4h)	1197 - 1547 ()	cubic $Pm\bar{3}m^{\dagger}$	Raevski <i>et al.</i> (2003) [27]
	1100 (4h)	1300 ()	cubic $Fm\bar{3}m$	Shuvaeva <i>et al.</i> (2003) [65]
	1200 (24h)	1350 ()	cubic $Fm\bar{3}m$	Rama <i>et al.</i> (2004) [21]
	997 - 1097 (4h)	1150 ()	cubic $Fm\bar{3}m^{\dagger}$	Demirbilek <i>et al.</i> (2004)
		1280 - 1350 ()	monoclinic	[28]
	800 - 1200 (4h)	1250 - 1400 (4h)	cubic $Fm\bar{3}m$	Eitssayeam <i>et al.</i> (2006)
				[24]
	800 - 1200 (4h)	1250 - 1400 (4h)	cubic $Fm\bar{3}m^{\ddagger}$	Eitssayeam <i>et al.</i> (2009)
				[23]
	1200 (3h)	1350 (3h)	cubic $Pm\bar{3}m$	Wang <i>et al.</i> (2007) [22]
	1200 (5h)	1250 (4h)	cubic $Pm\bar{3}m$	Bhagat & Prasad (2010)
				[31]
Columbite precursor	1200 (4h)	1350 (4h)	cubic $Pm\bar{3}m$	Intatha <i>et al.</i> (2010) [37]
	1000 (2h) \rightarrow 1200 (2h)	1250 (4h)	cubic $Pm\bar{3}m$	Ganguly <i>et al.</i> (2011) [26]
	900 - 1200 (4h)	1000 - 1200 (2h)	cubic $Pm\bar{3}m$	Khopkar & Sahoo (2020)
				[38]
	950 (5h)	1200-1350 (4h)	monoclinic	Chung <i>et al.</i> (2004) [34]
	1200 (8 h)	1250, 1300, 1350 (6h)	monoclinic	Ke <i>et al.</i> (2008) [32]
	950 (5h)	1200-1300 (4h)	monoclinic	Chung <i>et al.</i> (2008) [36]
	1200 (8h)	1300 (6h)	cubic $Fm\bar{3}m$	Ke <i>et al.</i> (2009, 2013) [25, 53]
	1000 (8h)	1100 (8h)	cubic $Pm\bar{3}m$	Liao <i>et al.</i> (2010) [55]
	1200 (8h)	1300 (6h)	cubic $Pm\bar{3}m$	Ke <i>et al.</i> (2010) [54]
	1200 (8h)	1250 (4h)	cubic $Pm\bar{3}m$	This work
Traditional mixed oxide	1200 ()	1250,1300,1350 (\gtrsim 4h)*	monoclinic	Ke <i>et al.</i> (2008) [32]
Powder calcination	1250 (4h)	1350 (2-5h)	monoclinic	Bochenek <i>et al.</i> (2009) [33]
Chemical	1300 (12h)	1400 (4h)	monoclinic	Charoenthai <i>et al.</i> (2008)
				[29]
Sol-gel	550 - 850 (5h)	1100 -1250 (3h)	monoclinic	Chung <i>et al.</i> (2005) [35]
Mechanical triggering	—	—	monoclinic	Bochenek <i>et al.</i> (2015) [56]
Mechanochemical	—	—	cubic	Bochenek <i>et al.</i> (2018) [57]

† estimated from the discussion. Lattice parameters are not available.

‡ estimated from the lattice parameters provided.

* estimated value from a cooling rate of $5^{\circ}\text{C}/\text{min}$.

- [3] N. Labhasetwar, G. Saravanan, S. K. Megarajan, N. Manwar, R. Khobragade, P. Doggali, and F. Grasset, "Perovskite-type catalytic materials for environmental applications," *Science and technology of advanced materials* **16**, 036002 (2015).
- [4] A. Kostopoulou, E. Kymakis, and E. Stratakis, "Perovskite nanostructures for photovoltaic and energy storage devices," *Journal of Materials Chemistry A* **6**, 9765–9798 (2018).
- [5] L. Yang, X. Kong, F. Li, H. Hao, Z. Cheng, H. Liu, J.-F. Li, and S. Zhang, "Perovskite lead-free dielectrics for energy storage applications," *Progress in Materials Science* **102**, 72–108 (2019).
- [6] H. J. Snaith, "Present status and future prospects of perovskite photovoltaics," *Nature materials* **17**, 372–376 (2018).
- [7] M. Roknuzzaman, C. Zhang, K. K. Ostrikov, A. Du, H. Wang, L. Wang, and T. Tesfamichael, "Electronic and optical properties of lead-free hybrid double perovskites for photovoltaic and optoelectronic applications," *Scientific reports* **9**, 718 (2019).
- [8] R. J. Cava, "Dielectric materials for applications in microwave communications basis of a presentation given at materials discussion no. 3, 26–29 september, 2000, university of cambridge, uk," *Journal of Materials Chemistry* **11**, 54–62 (2001).
- [9] I. M. Reaney and D. Iddles, "Microwave dielectric ceramics for resonators and filters in mobile phone networks," *Journal of the American Ceramic Society* **89**, 2063–2072 (2006).
- [10] P. Davies, H. Wu, A. Borisevich, I. Molodetsky, and L. Farber, "Crystal chemistry of complex perovskites: New cation-ordered dielectric oxides," *Annu. Rev. Mater. Res.* **38**, 369–401 (2008).
- [11] G. Smolenskii and A. Agranovskaya, "Dielectric polarization of a number of complex compounds," *Soviet Physics-Solid State* **1**, 1429–1437 (1960).
- [12] A. Bokov and Z.-G. Ye, "Recent progress in relaxor ferroelectrics with perovskite structure," *Journal of materials science* **41**, 31–52 (2006).
- [13] D. Fu, H. Taniguchi, M. Itoh, and S. Mori, "Pb(mg_{1/3}nb_{2/3})o₃ (pmn) relaxor: Dipole glass or nano-domain ferroelectric?" in *Advances in Ferroelectrics*, edited by A. P. Barranco (IntechOpen, Rijeka, 2012) Chap. 3.
- [14] M. J. Cabral, S. Zhang, E. C. Dickey, and J. M. LeBeau, "Gradient chemical order in the relaxor Pb(Mg_{1/3}Nb_{2/3})O₃," *Applied Physics Letters* **112**, 082901 (2018).
- [15] R. Blinc, P. Cevc, A. Zorko, J. Holc, M. Kosec, Z. Trontelj, J. Pirnat, N. Dalal, V. Ramachandran, and J. Krzystek, "Electron paramagnetic resonance of magnetoelectric Pb(Fe_{1/2}Nb_{1/2})O₃," *Journal of applied physics* **101**, 033901 (2007).
- [16] M. Lente, J. Guerra, G. De Souza, B. Fraygola, C. Raigoza, D. Garcia, and J. Eiras, "Nature of the magnetoelectric coupling in multiferroic Pb(Fe_{1/2}Nb_{1/2})O₃ ceramics," *Physical Review B* **78**, 054109 (2008).
- [17] D. Bochenek and Z. Surowiak, "Applications of iron (III) nitrate to obtain the multiferroic Pb(Fe_{1/2}Nb_{1/2})O₃ ceramics by the sol–gel method," *Journal of Alloys and Compounds* **480**, 732–736 (2009).
- [18] K. Tezuka, K. Henmi, Y. Hinatsu, and N. M. Masaki, "Magnetic susceptibilities and mössbauer spectra of perovskites A₂FeNbO₆ (A= Sr, Ba)," *Journal of Solid State Chemistry* **154**, 591–597 (2000).
- [19] M. Yokosuka, "Dielectric dispersion of the complex perovskite oxide Ba(Fe_{1/2}Nb_{1/2})O₃ at low frequencies," *Japanese journal of applied physics* **34**, 5338 (1995).
- [20] S. Saha and T. Sinha, "Structural and dielectric studies of BaFe_{0.5}Nb_{0.5}O₃," *Journal of Physics: Condensed Matter* **14**, 249 (2001).
- [21] N. Rama, J. Philipp, M. Opel, K. Chandrasekaran, V. Sankaranarayanan, R. Gross, and M. R. Rao, "Study of magnetic properties of A₂BNbO₆ (A= Ba, Sr, BaSr; and B = Fe and Mn) double perovskites," *Journal of applied physics* **95**, 7528–7530 (2004).
- [22] Z. Wang, X. Chen, L. Ni, and X. Liu, "Dielectric abnormalities of complex perovskite Ba(Fe_{1/2}Nb_{1/2})O₃ ceramics over broad temperature and frequency range," *Applied physics letters* **90**, 022904 (2007).
- [23] S. Eitssayeam, U. Intatha, K. Pengpat, G. Rujijanagul, K. MacKenzie, and T. Tunkasiri, "Effect of the solid-state synthesis parameters on the physical and electronic properties of perovskite-type Ba(Fe,Nb)_{0.5}O₃ ceramics," *Current Applied Physics* **9**, 993–996 (2009).
- [24] S. Eitssayeam, U. Intatha, K. Pengpat, and T. Tunkasiri, "Preparation and characterization of barium iron niobate (BaFe_{0.5}Nb_{0.5}O₃) ceramics," *Current Applied Physics* **6**, 316–318 (2006).
- [25] S. Ke, P. Lin, H. Fan, H. Huang, and X. Zeng, "Variable-range-hopping conductivity in high-κ Ba(Fe_{0.5}Nb_{0.5})O₃ ceramics," *Journal of Applied Physics* **114**, 104106 (2013).
- [26] M. Ganguly, S. Parida, E. Sinha, S. Rout, A. Himanshu, A. Husain, and I. Kim, "Structural, dielectric and electrical properties of BaFe_{0.5}Nb_{0.5}O₃ ceramic prepared by solid-state reaction technique," *Materials Chemistry and physics* **131**, 535–539 (2011).
- [27] I. Raevski, S. Prosandeev, A. Bogatin, M. Malitskaya, and L. Jastrabik, "High dielectric permittivity in AFe_{1/2}B_{1/2}O₃ nonferroelectric perovskite ceramics (A= Ba, Sr, Ca; B= Nb, Ta, Sb)," *Journal of applied physics* **93**, 4130–4136 (2003).
- [28] R. Demirbilek, A. I. A. Kutsenko, S. Kapphann, I. Raevski, S. Prosandeev, B. Burton, L. Jastrabik, and V. Vikhnin, "Optical spectra, properties and first principles computations of Ba(Fe,Nb)O₃ and Pb(Fe,Nb)O₃," *Ferroelectrics* **302**, 279–283 (2004).
- [29] N. Charoenthai, R. Traiphol, and G. Rujijanagul, "Microwave synthesis of barium iron niobate and dielectric properties," *Materials Letters* **62**, 4446–4448 (2008).
- [30] I. Raevski, S. Kubrin, S. Raevskaya, V. Titov, D. Sarychev, M. Malitskaya, I. Zakharchenko, and S. Prosandeev, "Experimental evidence of the crucial role of nonmagnetic Pb cations in the enhancement of the Néel temperature in perovskite Pb_{1-x}Ba_xFe_{1/2}Nb_{1/2}O₃," *Phys. Rev. B* **80**, 024108 (2009).
- [31] S. Bhagat and K. Prasad, "Structural and impedance spectroscopy analysis of Ba(Fe_{1/2}Nb_{1/2})O₃ ceramic," *Physica Status Solidi (a)* **207**, 1232–1239 (2010).
- [32] S. Ke, H. Huang, H. Fan, H. Chan, and L. Zhou, "Colossal dielectric response in barium iron niobate ceramics obtained by different precursors," *Ceramics international* **34**, 1059–1062 (2008).
- [33] D. Bochenek, Z. Surowiak, and J. Poltirova-Vejpravova, "Producing the lead-free BaFe_{0.5}Nb_{0.5}O₃ ceramics with multiferroic properties," *Journal of Alloys and Compounds* **487**, 572–576 (2009).
- [34] C.-Y. Chung, Y.-H. Chang, and G.-J. Chen, "Effects of lanthanum doping on the dielectric properties of Ba(Fe_{0.5}Nb_{0.5})O₃ ceramic," *Journal of applied physics* **96**, 6624–6628 (2004).
- [35] C.-Y. Chung, Y.-H. Chang, G.-J. Chen, and Y.-L. Chai, "Preparation, structure and ferroelectric properties of Ba(Fe_{0.5}Nb_{0.5})O₃ powders by sol–gel method," *Journal of crystal growth* **284**, 100–107 (2005).
- [36] C.-Y. Chung, Y.-S. Chang, G.-J. Chen, C.-C. Chung, and T.-W. Huang, "Effects of bismuth doping on the dielectric prop-

- erties of $\text{Ba}(\text{Fe}_{0.5}\text{Nb}_{0.5})\text{O}_3$ ceramic,” *Solid State Communications* **145**, 212–217 (2008).
- [37] U. Intatha, S. Eitssayeam, J. Wang, and T. Tunkasiri, “Impedance study of giant dielectric permittivity in $\text{BaFe}_{0.5}\text{Nb}_{0.5}\text{O}_3$ perovskite ceramic,” *Current Applied Physics* **10**, 21–25 (2010).
- [38] V. Khopkar and B. Sahoo, “Low temperature dielectric properties and NTCR behavior of the $\text{BaFe}_{0.5}\text{Nb}_{0.5}\text{O}_3$ double perovskite ceramic,” *Physical Chemistry Chemical Physics* **22**, 2986–2998 (2020).
- [39] P. Krishna, A. Shinde, A. Das, S. Naik, S. Paranjpe, and M. Ramanadham, “A multi PSD based medium resolution powder diffractometer,” *Solid State Physics (India)* **45**, 149 (2002).
- [40] J. Rodríguez-Carvajal, “Recent advances in magnetic structure determination by neutron powder diffraction,” *Physica B: Condensed Matter* **192**, 55–69 (1993).
- [41] E. Davis and N. Mott, “Conduction in non-crystalline systems V. conductivity, optical absorption and photoconductivity in amorphous semiconductors,” *Philosophical Magazine* **22**, 0903–0922 (1970).
- [42] R. Ray, A. Himanshu, P. Sen, U. Kumar, M. Richter, and T. Sinha, “Effects of octahedral tilting on the electronic structure and optical properties of d^0 double perovskites A_2ScSbO_6 (A= Sr, Ca),” *Journal of Alloys and Compounds* **705**, 497–506 (2017).
- [43] D. G. Barton, M. Shtein, R. D. Wilson, S. L. Soled, and E. Iglesia, “Structure and electronic properties of solid acids based on tungsten oxide nanostructures,” *The Journal of Physical Chemistry B* **103**, 630–640 (1999).
- [44] S. Basu, C. Nayak, A. K. Yadav, A. Agrawal, A. K. Poswal, D. Bhattacharyya, S. N. Jha, and N. K. Sahoo, “A comprehensive facility for EXAFS measurements at the INDUS-2 synchrotron source at RRCAT, indore, india,” *Journal of Physics: Conference Series* **493**, 012032 (2014).
- [45] A. Poswal, A. Agrawal, A. Yadav, C. Nayak, S. Basu, S. Kane, C. Garg, D. Bhattacharyya, S. Jha, and N. Sahoo, “Commissioning and first results of scanning type EXAFS beamline (BL-09) at INDUS-2 synchrotron source,” in *AIP Conference Proceedings*, Vol. 1591 (AIP, 2014) pp. 649–651.
- [46] D. C. Koningsberger and R. Prins, *X-ray absorption: principles, applications, techniques of EXAFS, SEXAFS and XANES* (Wiley/Interscience, New York, 1988).
- [47] S. D. Kelly, D. Hesterberg, and B. Ravel, “Analysis of soils and minerals using x-ray absorption spectroscopy,” in *Methods of Soil Analysis Part 5—Mineralogical Methods* (John Wiley & Sons, Ltd, 2008) Chap. 14, pp. 387–463, <https://access.onlinelibrary.wiley.com/doi/pdf/10.2136/sssabookser5.5.c1>
- [48] M. Newville, B. Ravel, D. Haskel, J. Rehr, E. Stern, and Y. Yacoby, “Analysis of multiple-scattering XAFS data using theoretical standards,” *Physica B: Condensed Matter* **208**, 154–156 (1995).
- [49] R. Morrow, M. I. Sturza, R. Ray, C. Hincinschi, J. Kern, P. Schlender, M. Richter, S. Wurmehl, and B. Büchner, “Discovery, crystal growth, and characterization of garnet $\text{Eu}_2\text{PbSb}_2\text{Zn}_3\text{O}_{12}$,” *European Journal of Inorganic Chemistry* **2020**, 2512–2520 (2020).
- [50] J. P. Perdew, K. Burke, and M. Ernzerhof, “Generalized gradient approximation made simple,” *Phys. Rev. Lett.* **77**, 3865–3868 (1996).
- [51] P. Blaha, K. Schwarz, G. K. Madsen, D. Kvasnicka, and J. Luitz, “WIEN2k,” An augmented plane wave+ local orbitals program for calculating crystal properties (2001).
- [52] V. I. Anisimov, I. Solovyev, M. Korotin, M. Czyżyk, and G. Sawatzky, “Density-functional theory and NiO photoemission spectra,” *Physical Review B* **48**, 16929 (1993).
- [53] S. Ke, H. Fan, and H. Huang, “Dielectric relaxation in A_2FeNbO_6 (A= Ba, Sr, and Ca) perovskite ceramics,” *Journal of electroceramics* **22**, 252–256 (2009).
- [54] S. Ke and H. Huang, “Giant low frequency dielectric tunability in high-k $\text{BaFe}_{1/2}\text{Nb}_{1/2}\text{O}_3$ ceramics at room temperature,” *Journal of applied physics* **108**, 064104 (2010).
- [55] K.-F. Liao, Y.-S. Chang, Y.-L. Chai, Y.-Y. Tsai, and H.-L. Chen, “Structure and dielectric properties of sodium-doped $\text{Ba}(\text{FeNb})_{0.5}\text{O}_3$,” *Materials Science and Engineering: B* **172**, 300–304 (2010).
- [56] D. Bochenek, P. Niemiec, I. Szafraniak-Wiza, M. Adamczyk, and R. Skulski, “Preparation and dielectric properties of the lead-free $\text{BaFe}_{1/2}\text{Nb}_{1/2}\text{O}_3$ ceramics obtained from mechanically triggered powder,” *The European Physical Journal B* **88**, 277 (2015).
- [57] D. Bochenek, P. Niemiec, M. Adamczyk, and I. Szafraniak-Wiza, “Physical properties of lead-free $\text{BaFe}_{1/2}\text{Nb}_{1/2}\text{O}_3$ ceramics obtained from mechanochemically synthesized powders,” *Journal of Materials Science* **53**, 13501–13512 (2018).
- [58] O. Raymond, R. Font, N. Suarez, J. Portelles, and J. Siqueiros, “Effects of two kinds of FeNbO_4 precursors in the obtainment and dielectric properties of PFN ceramics,” *Ferroelectrics* **294**, 141–154 (2003).
- [59] P. W. Barnes, M. W. Lufaso, and P. M. Woodward, “Structure determination of $\text{A}_2\text{M}^{3+}\text{TaO}_6$ and $\text{A}_2\text{M}^{3+}\text{NbO}_6$ ordered perovskites: octahedral tilting and pseudosymmetry,” *Acta Crystallographica Section B: Structural Science* **62**, 384–396 (2006).
- [60] G. Cao, T. F. Qi, L. Li, J. Terzic, S. J. Yuan, L. E. DeLong, G. Murthy, and R. K. Kaul, “Novel magnetism of $\text{Ir}^{5+}(5d^4)$ ions in the double perovskite Sr_2YIrO_6 ,” *Phys. Rev. Lett.* **112**, 056402 (2014).
- [61] L. T. Corredor, G. Aslan-Cansever, M. Sturza, K. Manna, A. Maljuk, S. Gass, T. Dey, A. U. B. Wolter, O. Kataeva, A. Zimmermann, M. Geyer, C. G. F. Blum, S. Wurmehl, and B. Büchner, “Iridium double perovskite Sr_2YIrO_6 : A combined structural and specific heat study,” *Phys. Rev. B* **95**, 064418 (2017).
- [62] I. Raevski, S. Kuropatkina, S. Kubrin, S. Raevskaya, V. Titov, D. Sarychev, M. Malitskaya, A. Bogatin, and I. Zakharchenko, “Dielectric and mössbauer studies of high-permittivity $\text{BaFe}_{1/2}\text{Nb}_{1/2}\text{O}_3$ ceramics with cubic and monoclinic perovskite structures,” *Ferroelectrics* **379**, 48–54 (2009).
- [63] C. J. Bartel, C. Sutton, B. R. Goldsmith, R. Ouyang, C. B. Musgrave, L. M. Ghiringhelli, and M. Scheffler, “New tolerance factor to predict the stability of perovskite oxides and halides,” *Science advances* **5**, eaav0693 (2019).
- [64] J. M. Tranquada, S. M. Heald, and A. R. Moodenbaugh, “X-ray-absorption near-edge-structure study of $\text{La}_{2-x}\text{Ba}_x\text{CuO}_{4-y}$ superconductors,” *Phys. Rev. B* **36**, 5263–5274 (1987).
- [65] V. Shuvaeva, I. Raevski, O. Polozhentsev, Y. V. Zubavichus, V. Vlasenko, S. Raevskaya, and H. Chen, “The Fe k-edge x-ray absorption study of the local structure of $\text{BaFe}_{0.5}\text{Nb}_{0.5}\text{O}_3$,” *Materials Chemistry and Physics* **193**, 260–266 (2017).
- [66] C. Bharti, A. Dutta, S. Shannigrahi, and T. Sinha, “Electronic structure, magnetic and electrical properties of multi-ferroic $\text{PbFe}_{1/2}\text{Ta}_{1/2}\text{O}_3$,” *Journal of Magnetism and Magnetic Materials* **324**, 955–960 (2012).
- [67] A. Kumar, A. Chaudhary, K. Gautam, and D. Pandey, “Magnetic ground state and crystal structure of the giant dielectric constant material $\text{Ba}(\text{Fe}_{1/2}\text{Nb}_{1/2})\text{O}_3$,” *Journal of Magnetism and Magnetic Materials* **537**, 168236 (2021).